

Disconnect to Connect: A Data Augmentation Method for Improving Topology Accuracy in Image Segmentation

Juan Miguel Valverde^{1,2,3} Maja Østergaard³ Adrian Rodriguez-Palomo³
 Peter A. S. Vibe³ Nina K. Wittig³ Henrik Birkedal³ Anders Bjorholm Dahl¹

¹DTU Compute, Technical University of Denmark, Denmark

²A.I. Virtanen Institute, University of Eastern Finland, Finland

³Department of Chemistry and iNANO, Aarhus University, Denmark

{jmvma,abda}@dtu.dk {majaoester,adrian.rodriquez,petervibe}@inano.au.dk hbirkedal@chem.au.dk

Abstract

Accurate segmentation of thin, tubular structures (e.g., blood vessels) is challenging for deep neural networks. These networks classify individual pixels, and even minor misclassifications can break the thin connections within these structures. Existing methods for improving topology accuracy, such as topology loss functions, rely on very precise, topologically-accurate training labels, which are difficult to obtain. This is because annotating images, especially 3D images, is extremely laborious and time-consuming. Low image resolution and contrast further complicates the annotation by causing tubular structures to appear disconnected. We present CoLeTra, a data augmentation strategy that integrates to the models the prior knowledge that structures that appear broken are actually connected. This is achieved by creating images with the appearance of disconnected structures while maintaining the original labels. Our extensive experiments, involving different architectures, loss functions, and datasets, demonstrate that CoLeTra leads to segmentations topologically more accurate while often improving the Dice coefficient and Hausdorff distance. CoLeTra’s hyper-parameters are intuitive to tune, and our sensitivity analysis shows that CoLeTra is robust to changes in these hyper-parameters. We also release a dataset specifically suited for image segmentation methods with a focus on topology accuracy. CoLeTra’s code can be found at <https://github.com/jmlipman/CoLeTra>.

1. Introduction

Despite the remarkable potential of deep learning for image segmentation [26], accurate segmentation of thin, tubular structures, such as axons, airways, and blood vessels,

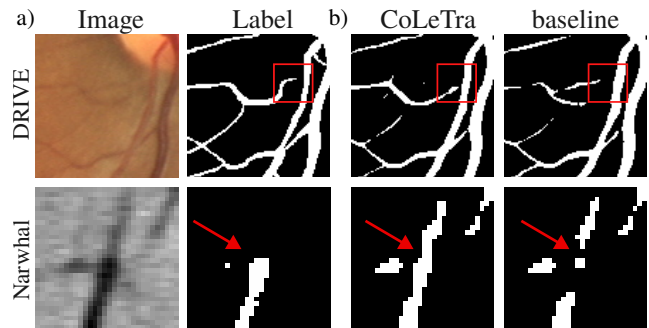


Figure 1. a) Labels missing important areas, compromising the structure’s true topology. b) CoLeTra yields segmentations topologically more accurate.

remains a significant challenge. This is partly due to the inherent pixel-wise¹ classification nature of standard deep learning models, where small misclassifications that hardly increase the loss, can lead to segmentations with discontinuities, impairing the quantification [14]. For instance, connected-component analysis of structures with broken connections would misinterpret each fragment as a distinct structure, resulting in overestimating their number. An incorrect number of connected components would then compromise other measurements, such as average length, density, and directionality.

An important line of research has focused on emphasizing regions’ connectedness with topology loss functions [4, 13, 14, 20, 42]. These are loss functions that aim to produce segmentations that match the number of connected components, 1D holes, and 2D cavities of the ground truth, i.e., the Betti numbers [7]. An advantage of these methods is that they offer straightforward integration into existing

¹Throughout this paper, we will use the terms *pixel* and *voxel* exchangeably.

deep learning frameworks. However, these topology loss functions require very accurate labels, an often unrealistic requirement in areas such as medical imaging and material science [39]. Due to the low image resolution and contrast, it is challenging to annotate the images because the tubular structures may appear disconnected (see Fig. 1). In these cases, the loss functions inadvertently reinforce the absence of a structure that we know should exist based on prior knowledge about connectivity. Alternatively, regions’ connectedness can also be enhanced by incorporating such prior knowledge into the models. This has been achieved by integrating domain knowledge through dataset-specific data augmentation [46, 50], but this is designed for each problem and is not generally applicable.

In this paper, we present CoLeTra, the first, to the best of our knowledge, data augmentation method specifically created for improving topology accuracy in image segmentation. CoLeTra uses image inpainting to artificially create images with the appearance of disconnected tubular structures while keeping the ground truth labels as they are (see Fig. 2), encouraging the model to learn that structures that appear disconnected are actually connected. We show with extensive experiments on four datasets, two architectures, and six loss functions that this simple strategy generally leads to segmentations with more accurate topology, *i.e.*, segmentations with the number of connected components and holes more similar to the ground truth. CoLeTra can be easily incorporated into existing training pipelines, and, importantly, it can be utilized jointly with other methods that consider topology, such as topology loss functions, as well as with other data augmentations. Furthermore, CoLeTra adds only a negligible overhead during the optimization and, unlike other topology-enhancing strategies [12, 13, 42], it requires no extra GPU memory. Specifically, our contributions are the following:

- We present the first data augmentation method for image segmentation that focuses on topology.
- Our method improves topology accuracy across a wide range of settings, even when optimizing topology loss functions.
- Our method is robust to changes in its two hyperparameters.
- We release a dataset ideally suited for evaluating image segmentation methods with an emphasis on topology accuracy. This dataset release aims to foster future research in the field.

2. Related work

Topology loss functions At the core of several loss functions that aim at topology accuracy, we find persistence homology [5]—a tool to analyze topological features. Particularly in image segmentation, persistent homology tracks how connected components, holes, and cavities appear and

disappear as all possible thresholds are applied to softmax probability values [11]. Although there are libraries that facilitate its computation, such as Gudhi [24], computing persistence homology on large images is very expensive, which has forced researchers to compute it on small image patches, thus, disregarding global topology. Hu *et al.* [13] developed a loss function that uses persistence homology to find topological features and encourage some of them to be preserved while others to be removed. Gabrielsson *et al.* [6] introduced a differentiable topology layer to incorporate topological priors in deep neural networks. Clough *et al.* [4] and Shin *et al.* [41] used persistence homology during training and at inference time to infuse a pre-specified type and number of topological features. Hu *et al.* [14] proposed a model that, with the help of Morse theory, learns a representation space of structures like branches, computes their saliency with persistence homology, and generates the predicted segmentations by sampling branches from that space. Byrne *et al.* [1] and He *et al.* [8] extended persistent homology losses to multi-class segmentation, and Oner *et al.* [32] employed a novel filtration technique, utilized by persistence homology to identify topological features, that combines approaches from topological data analysis.

In parallel to this trend, other topology loss functions do not rely on calculating persistence homology. Hu *et al.* [12] proposed to correct the critical points, *i.e.*, the pixels that change the topology of the segmentation to the desired one. This method, however, requires computing distance maps several times, slowing down the training considerably. Liao [20] developed a method based on Dijkstra’s algorithm that is also reportedly expensive to compute. Shi *et al.* [42] presented “centerline Dice loss” (clDice), which, through a novel differentiable skeletonization algorithm, focuses on achieving accurate skeletons of the region of interest. Although this method is faster to compute than the aforementioned loss functions, it requires larger GPU memory. More recently, Shi *et al.* [40] and Kirchhoff *et al.* [18] also presented topology loss functions that emphasize performance in the centerline area.

Prior knowledge via data augmentation Data augmentation can integrate prior knowledge into the models during training by leveraging domain-specific knowledge. In one example, the medical knowledge that tumors can grow in different locations has been incorporated by randomly flipping the images during the optimization [28]. In another example, intra and inter-rater variability was simulated by applying random deformations to the segmentation mask boundaries [16]. In other domains, Yang *et al.* [50] proposed a data augmentation transformation to create defects in metal surfaces accounting for new defect types that only appeared in the test set. Teshima *et al.* [46] incorporated prior knowledge of conditional independence relations for

predictive modeling with data augmentation.

Inpainting to increase generalizability Image inpainting is used for reconstructing missing parts of an image, *e.g.*, to replace a removed object. However, a range of other applications have emerged. Inpainting has been used as a self-supervised learning task to achieve models with better feature representations. Pathak *et al.* [33] and Zhong *et al.* [56] trained models to reconstruct areas filled with random values; Chen *et al.* [3] reconstructed images with swapped random patches; and Li *et al.* [19] focused on reconstructing the most discriminative regions. Another line of research employs image inpainting to achieve larger, more diverse training sets. These approaches use off-the-shelf image inpainting methods to create “background images”, where objects have been removed, for later to place other objects on those background images. Ruiz *et al.* [36, 37] proposed a method that decides with k -nearest neighbors which object to put in the inpainted background images. Zhang *et al.* [55] trained a model named PlaceNet that predicts potential object locations and scales within the background images. Wang *et al.* [48] developed a method that determines objects’ location via a genetic algorithm. Nie *et al.* [30] focused on creating synthetic datasets for pedestrian detection. Saha *et al.* [38] approach detects vehicles with a Mask RCNN [9] and removes them via inpainting. More recently, He *et al.* [10] used image inpainting to generate images with objects from the minority class to tackle class imbalance. In this paper, we use image inpainting to augment data with appearance of change in topology.

3. Method

In this section, we present our **Continuity Learning Transformation (CoLeTra)** to improve topology accuracy by learning to connect discontinuous structures via data augmentation. Let $\mathbf{x} \in \mathbb{R}^d$ be an image of d pixels from a training mini-batch, and let $\mathbf{y} \in \{0, 1\}^d$ be its corresponding ground-truth segmentation mask. CoLeTra transforms \mathbf{x} during training:

$$x_p \leftarrow g(p, c, \sigma)\tilde{x}_p + (1 - g(p, c, \sigma))x_p \quad (1)$$

$$\forall p \in \varphi(c, s), \forall c \in C,$$

where $C = \{c_1, \dots, c_n\}$ is a set of n pixel coordinates such that $y_{c_i} = 1$; $\tilde{\mathbf{x}}$ is an inpainted version of \mathbf{x} with all the thin structures removed; $\varphi(c, s)$ is the set of pixel coordinates within a window size of $s \times s$ centered at c ; and $g(p, c, \sigma) = \exp(-\frac{1}{2} \frac{\|p-c\|_2^2}{\sigma^2}) \in [0, 1]$ is the value of a Gaussian kernel that weighs the contribution of $\tilde{\mathbf{x}}$ and \mathbf{x} at pixel p . For the sake of clarity, we simplified our notation; CoLeTra extends naturally to multi-class classification, and, as our experiments show, to multi-channel n -dimensional

images. Figure 2 illustrates our method. Intuitively, CoLeTra erases random parts of the tubular structures via image inpainting while leaving the ground truth as it is. This simple yet effective method aims to teach the models that, although the structures may not appear connected, they are.

CoLeTra is designed to be simple. It is agnostic to the inpainting method, allowing it to always utilize state-of-the-art inpainting methods and inpainting methods that are more suitable for specific datasets. In our implementation, we used LaMa [45] to remove all tubular structures. To ensure smooth borders and complete coverage of thin structures, the areas for inpainting were defined by dilating the labels three times:

$$\tilde{\mathbf{x}} = \text{LaMa}(\mathbf{x}, \text{dilate}(\mathbf{y}, \text{times} = 3)). \quad (2)$$

CoLeTra also uses a simple method for finding where to artificially break the thin structures. During training, CoLeTra generates a set of random pixels by sampling, with the same probability, n pixels containing the structure to be segmented:

$$C \subset \{i : y_i = 1\} : |C| = n. \quad (3)$$

CoLeTra, then, centers the inpainted patches in each pixel belonging to the subset C .

CoLeTra’s simplicity provides two important benefits. First, CoLeTra only adds a negligible overhead (in the order of ms per iteration) to the training while requiring no extra GPU memory. Second, the strategy for finding where to disconnect structures can be tailored to each dataset based on prior knowledge. For instance, disconnections could be applied to areas with lower contrast or at points where structures bifurcate, prioritizing the correction of regions with these specific characteristics. In this work, we show in different datasets that, even with a simple strategy, CoLeTra achieves segmentations topologically more accurate.

4. Experiments

4.1. CoLeTra connects disconnected tubular structures

To mimic a standard image quantification pipeline, we created a synthetic dataset where the ultimate goal was to count the number of thin, tubular structures via connected-component analysis. The dataset consisted of two greyscale images: one for training a segmentation model, and one for validation. The training image contained five solid black lines, while the validation image contained two solid and two dashed lines, simulating, what often occurs in medical imaging and imaging for material science, that structures may appear unconnected due to the low contrast and/or limited voxel resolution (see Fig. 3 (top)). This setup is challenging since the training image does not contain any struc-

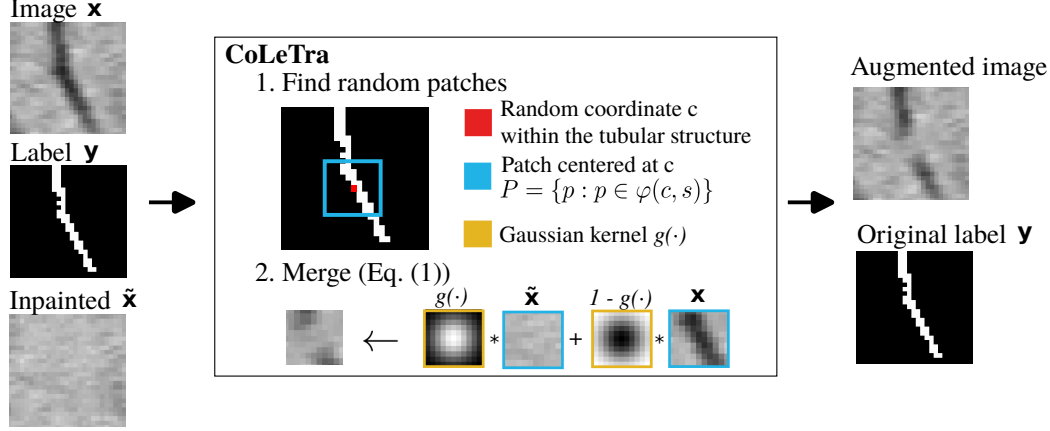


Figure 2. Overview of CoLeTra data augmentation.

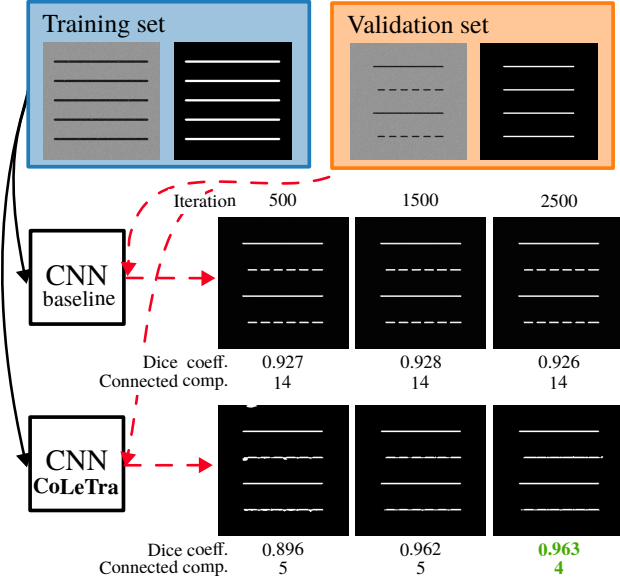


Figure 3. CoLeTra incorporates prior knowledge about structures' connectedness. Top: training and validation set images from the synthetic dataset. Bottom: Results in the validation set, where top/bottom is without/with CoLeTra.

ture discontinuity. To tackle this task, we trained two DynUNet² models: one with and one without CoLeTra, both with the same training configuration.

The model trained with CoLeTra learned to connect the dashed lines (see Fig. 3 (right, bottom)), facilitating the subsequent connected-component analysis of the segmentation mask. In contrast, the model trained without CoLeTra yielded segmentations with incorrect topology (see Fig. 3 (right, center)). This experiment shows that CoLeTra can incorporate, during training, the prior knowledge that structures in the test/validation images must be connected when

they appear unconnected, even if such information was not in the original training set.

4.2. CoLeTra improves topology accuracy on different settings

Datasets and data split. We evaluated CoLeTra on four datasets: DRIVE (CC-BY-4.0) [44], Crack500 [51], CREMI³, and the Narwhal dataset—that we make publicly available. The DRIVE [44] dataset comprised 20 fundus retina images collected for diabetic retinopathy detection, and the segmentation task focused on blood vessel segmentation. Due to the small dataset size, we conducted three-fold cross validation, and we further applied a 0.8:0.2 split to yield the training and validation sets. The Crack500 [51] dataset included 500 images with pavement cracks, for which we utilized the original training, validation, test set splits of 250, 50, and 200 images, respectively. The CREMI dataset contained three 3D electron-microscopy images from adult *Drosophila melanogaster* brain tissue. The task was to segment the borders between the neurons and, as in the DRIVE dataset experiments, we conducted a three-fold cross-validation, assigning one image to the training set, one image to the validation set, and the remaining image to the test set. The Narwhal dataset comprised synchrotron 3D images from a narwhal tusk, where the task was to segment the dentine tubules. The dataset consisted of 20 patches from a single scan for training, one patch from a different scan for validation, and three patches from other scans for testing. For details about the Narwhal dataset and where to download it, we refer to Appendix A.

Experimental setup We investigated the advantageousness of CoLeTra in 48 different scenarios, combining two architectures, six loss functions, and the four datasets mentioned above. We trained a DynUNet, which is based on

²<https://docs.monai.io/en/stable/networks.html#dynunet>

³<https://cremi.org>

		DynUNet				AttentionUNet				
		Betti	cIDice	Dice	HD95	Betti	cIDice	Dice	HD95	
DRIVE	CE	baseline	3.687 (0.581)	0.683 (0.006)	0.709 (0.005)	8.379 (0.654)	3.925 (0.431)	0.681 (0.008)	0.712 (0.006)	7.273 (0.590)
		+DA	1.334 (0.128)	0.700 (0.007)	0.726 (0.004)	8.392 (0.676)	1.421 (0.149)	0.707 (0.007)	0.731 (0.005)	6.650 (0.461)
		+DA+CoLeTra	1.282 (0.109)	0.701 (0.006)	0.725 (0.005)	8.305 (0.710)	1.390 (0.155)	0.709 (0.007)	0.731 (0.005)	6.637 (0.499)
	Dice	baseline	3.952 (0.345)	0.683 (0.006)	0.714 (0.005)	7.416 (0.401)	2.619 (0.462)	0.700 (0.004)	0.726 (0.003)	6.802 (0.468)
		+DA	1.226 (0.119)	0.718 (0.005)	0.737 (0.004)	7.120 (0.539)	0.974 (0.189)	0.734 (0.009)	0.749 (0.006)	6.212 (0.403)
		+DA+CoLeTra	1.149 (0.110)	0.720 (0.006)	0.737 (0.005)	6.987 (0.483)	0.930 (0.156)	0.734 (0.006)	0.747 (0.005)	6.186 (0.588)
	RWLoss	baseline	3.224 (0.531)	0.682 (0.009)	0.711 (0.008)	8.028 (0.588)	2.758 (0.378)	0.694 (0.008)	0.723 (0.003)	7.092 (0.504)
		+DA	0.992 (0.075)	0.730 (0.006)	0.744 (0.004)	7.952 (0.646)	0.815 (0.119)	0.738 (0.004)	0.750 (0.003)	7.171 (0.713)
		+DA+CoLeTra	0.984 (0.076)	0.729 (0.005)	<u>0.744</u> (0.003)	7.717 (0.565)	0.806 (0.100)	0.738 (0.007)	<u>0.750</u> (0.005)	7.095 (0.840)
	cIDice	baseline	3.597 (0.469)	0.690 (0.008)	0.715 (0.006)	7.158 (0.436)	1.889 (0.261)	0.715 (0.007)	0.725 (0.004)	6.994 (0.853)
		+DA	0.747 (0.084)	0.745 (0.004)	0.738 (0.003)	6.522 (0.500)	0.657 (0.068)	<u>0.765</u> (0.004)	0.748 (0.003)	5.784 (0.369)
		+DA+CoLeTra	0.741 (0.084)	0.746 (0.004)	0.735 (0.003)	6.641 (0.425)	0.664 (0.083)	0.764 (0.004)	0.747 (0.003)	5.883 (0.407)
	Warploss	baseline	3.982 (0.413)	0.680 (0.007)	0.713 (0.005)	7.583 (0.472)	2.592 (0.454)	0.700 (0.004)	0.726 (0.002)	6.808 (0.463)
		+DA	1.211 (0.105)	0.718 (0.005)	0.737 (0.004)	7.109 (0.567)	0.974 (0.189)	0.734 (0.009)	0.749 (0.006)	6.212 (0.403)
		+DA+CoLeTra	1.166 (0.103)	0.720 (0.006)	0.737 (0.005)	6.930 (0.502)	0.937 (0.159)	0.734 (0.005)	0.747 (0.004)	6.244 (0.593)
	Topoloss	baseline	3.631 (0.494)	0.682 (0.007)	0.709 (0.006)	8.350 (0.586)	4.151 (0.512)	0.680 (0.009)	0.711 (0.007)	7.347 (0.687)
		+DA	1.310 (0.132)	0.700 (0.008)	0.726 (0.005)	8.415 (0.728)	1.421 (0.149)	0.707 (0.007)	0.731 (0.005)	6.650 (0.461)
		+DA+CoLeTra	1.291 (0.108)	0.701 (0.006)	0.725 (0.005)	8.379 (0.793)	1.412 (0.157)	0.708 (0.007)	0.731 (0.005)	6.666 (0.450)
Crack500	CE	baseline	0.187 (0.028)	0.718 (0.021)	0.650 (0.016)	81.581 (22.585)	0.184 (0.030)	0.716 (0.022)	0.649 (0.018)	79.359 (24.002)
		+DA	0.136 (0.019)	0.782 (0.016)	0.693 (0.014)	32.572 (9.285)	0.164 (0.032)	0.755 (0.025)	0.674 (0.023)	38.159 (9.276)
		+DA+CoLeTra	0.132 (0.017)	0.786 (0.015)	0.697 (0.014)	30.229 (6.827)	0.156 (0.031)	0.766 (0.023)	0.685 (0.021)	34.976 (10.205)
	Dice	baseline	0.179 (0.027)	0.726 (0.022)	0.653 (0.018)	63.756 (22.146)	0.176 (0.055)	0.738 (0.031)	0.662 (0.025)	59.935 (23.785)
		+DA	0.125 (0.014)	0.797 (0.013)	0.708 (0.010)	36.657 (8.018)	0.138 (0.021)	0.778 (0.020)	0.693 (0.019)	38.964 (9.397)
		+DA+CoLeTra	0.124 (0.012)	0.801 (0.012)	0.714 (0.010)	33.360 (9.483)	0.133 (0.017)	0.785 (0.017)	0.702 (0.015)	37.151 (7.439)
	RWLoss	baseline	0.164 (0.025)	0.728 (0.022)	0.649 (0.019)	71.526 (25.560)	0.156 (0.032)	0.746 (0.034)	0.664 (0.033)	51.660 (15.776)
		+DA	0.125 (0.012)	0.786 (0.013)	0.697 (0.011)	40.152 (11.967)	0.146 (0.030)	0.763 (0.024)	0.683 (0.023)	40.908 (11.928)
		+DA+CoLeTra	0.122 (0.013)	0.791 (0.014)	0.702 (0.013)	36.433 (10.352)	0.138 (0.023)	0.764 (0.018)	0.682 (0.015)	39.833 (10.875)
	cIDice	baseline	0.136 (0.016)	0.767 (0.019)	0.674 (0.017)	48.356 (18.612)	0.134 (0.021)	0.785 (0.039)	0.666 (0.036)	51.087 (27.508)
		+DA	0.126 (0.014)	0.826 (0.015)	0.704 (0.011)	36.459 (7.465)	0.134 (0.023)	0.808 (0.028)	0.679 (0.028)	45.971 (16.914)
		+DA+CoLeTra	0.128 (0.011)	0.831 (0.013)	0.708 (0.010)	33.686 (8.266)	0.129 (0.016)	0.811 (0.027)	0.671 (0.031)	48.804 (17.778)
	Warploss	baseline	0.180 (0.029)	0.725 (0.021)	0.653 (0.017)	65.101 (21.753)	0.174 (0.053)	0.736 (0.033)	0.659 (0.026)	61.219 (23.147)
		+DA	0.125 (0.013)	0.798 (0.013)	0.708 (0.011)	36.826 (8.713)	0.138 (0.021)	0.778 (0.020)	0.693 (0.019)	38.964 (9.397)
		+DA+CoLeTra	0.124 (0.012)	0.800 (0.013)	0.713 (0.011)	37.629 (7.824)	0.134 (0.019)	0.783 (0.016)	0.700 (0.015)	37.879 (9.581)
	Topoloss	baseline	0.189 (0.032)	0.718 (0.020)	0.651 (0.017)	80.855 (22.609)	0.182 (0.029)	0.716 (0.021)	0.649 (0.017)	77.987 (21.952)
		+DA	0.135 (0.018)	0.782 (0.016)	0.693 (0.014)	32.176 (8.028)	0.164 (0.032)	0.755 (0.025)	0.674 (0.023)	38.159 (9.276)
		+DA+CoLeTra	0.133 (0.018)	0.785 (0.016)	0.697 (0.015)	30.677 (6.195)	0.162 (0.031)	0.761 (0.023)	0.682 (0.021)	34.673 (8.231)
CREMI	CE	baseline	32995.333 (906.375)	0.969 (0.000)	0.977 (0.000)	0.021 (0.001)	<u>19023.778</u> (2184.153)	0.969 (0.000)	0.971 (0.001)	0.031 (0.001)
		+DA	37514.333 (470.435)	0.971 (0.000)	0.980 (0.000)	0.010 (0.000)	23239.889 (3385.695)	0.964 (0.004)	0.972 (0.002)	0.024 (0.002)
		+DA+CoLeTra	36150.444 (864.843)	0.971 (0.000)	0.979 (0.000)	0.014 (0.000)	23690.222 (5848.199)	0.965 (0.002)	0.970 (0.001)	0.034 (0.002)
	Dice	baseline	31676.556 (471.876)	0.969 (0.000)	0.977 (0.000)	0.019 (0.000)	23081.778 (2526.715)	0.970 (0.001)	0.972 (0.000)	0.033 (0.001)
		+DA	38809.111 (888.314)	0.972 (0.000)	0.980 (0.000)	0.010 (0.000)	36768.889 (5455.327)	0.964 (0.005)	0.971 (0.002)	0.026 (0.003)
		+DA+CoLeTra	37319.333 (919.677)	0.971 (0.001)	0.979 (0.000)	0.016 (0.001)	34227.111 (5602.781)	0.966 (0.003)	0.971 (0.001)	0.031 (0.002)
	RWLoss	baseline	33455.111 (909.125)	0.969 (0.001)	0.977 (0.000)	0.019 (0.000)	22914.889 (2070.941)	0.970 (0.000)	0.971 (0.001)	0.034 (0.001)
		+DA	38493.000 (843.885)	0.971 (0.000)	0.980 (0.000)	0.011 (0.001)	36398.222 (5491.616)	0.965 (0.004)	0.972 (0.002)	0.025 (0.002)
		+DA+CoLeTra	36568.889 (1473.720)	0.971 (0.001)	0.979 (0.001)	0.017 (0.001)	34942.778 (5882.784)	0.966 (0.003)	0.971 (0.001)	0.028 (0.003)
	cIDice	baseline	33945.444 (770.907)	0.969 (0.000)	0.977 (0.000)	0.020 (0.001)	31580.667 (2925.908)	0.971 (0.001)	0.973 (0.000)	0.032 (0.001)
		+DA	41323.889 (1194.337)	0.970 (0.000)	0.979 (0.000)	0.015 (0.001)	46767.111 (3484.914)	0.962 (0.004)	0.967 (0.002)	0.033 (0.004)
		+DA+CoLeTra	40092.667 (632.833)	0.969 (0.001)	0.977 (0.001)	0.020 (0.001)	47320.111 (3686.082)	0.961 (0.003)	0.965 (0.002)	0.037 (0.003)
	Warploss	baseline	31639.889 (588.069)	0.969 (0.000)	0.977 (0.000)	0.019 (0.000)	22759.111 (2657.958)	0.970 (0.000)	0.972 (0.000)	0.033 (0.001)
		+DA	38704.667 (921.115)	0.972 (0.000)	0.980 (0.000)	0.010 (0.000)	36482.222 (5593.270)	0.965 (0.005)	0.971 (0.002)	0.027 (0.002)
		+DA+CoLeTra	37300.000 (886.955)	0.971 (0.000)	0.979 (0.000)	0.016 (0.001)	34594.889 (4623.187)	0.966 (0.004)	0.971 (0.002)	0.030 (0.003)
	Topoloss	baseline	32699.667 (728.942)	0.969 (0.000)	0.977 (0.000)	0.021 (0.000)	19208.778 (1974.309)	0.969 (0.000)	0.971 (0.000)	0.031 (0.001)
		+DA	37760.444 (986.411)	0.971 (0.000)	0.980 (0.000)	0.010 (0.000)	25475.111 (6668.060)	0.964 (0.004)	0.971 (0.002)	0.025 (0.002)
		+DA+CoLeTra	36387.444 (1036.850)	0.971 (0.000)	0.979 (0.000)	0.013 (0.000)	24241.667 (3969.347)	0.966 (0.002)	0.971 (0.001)	0.029 (0.002)
Narwhal	CE	baseline	12805.889 (787.121)	0.828 (0.008)	0.577 (0.022)	1.939 (0.078)	13814.444 (2379.275)	0.843 (0.010)	0.627 (0.035)	1.713 (0.111)
		+DA	9907.778 (1128.195)	0.855 (0.013)	0.671 (0.050)	1.801 (0.147)	24430.778 (4492.010)	0.834 (0.020)	0.701 (0.031)	1.844 (0.277)
		+DA+CoLeTra	8988.556 (429.358)	0.851 (0.014)	0.686 (0.044)	1.861 (0.197)	16806.000 (4805.655)	0.851 (0.007)	0.726 (0.010)	1.748 (0.087)
	Dice	baseline	20779.889 (1659.472)	0.681 (0.051)	0.327 (0.041)	3.354 (0.470)	25869.667 (2713.092)	0.759 (0.075)	0.458 (0.177)	2.467 (0.542)
		+DA	20280.111 (249.327)	0.670 (0.019)	0.314 (0.004)	3.235 (0.148)	20969.444 (4201.928)	0.775 (0.066)	0.494 (0.167)	2.607 (0.645)
		+DA+CoLeTra	18457.111 (1220.830)	0.663 (0.028)	0.318 (0.020)	3.451 (0.290)	24830.111 (10180.901)	0.738 (0.087)	0.465 (0.146)	2.824 (0.652)
	RWLoss	baseline	20010.444 (5278.833)	0.774 (0.017)	0.529 (0.042)	2.362 (0.177)	17789.111 (16530.243)	0.818 (0.034)	0.526 (0.154)	2.013 (0.343)
		+DA	12697.000 (2712.586)	0.833 (0.003)	0.632 (0.020)	2.014 (0.064)	8112.333 (4885.627)	0.837 (0.040)	0.545 (0.182)	2.136 (0.511)
		+DA+CoLeTra	13046.778 (3102.622)	0.829 (0.002)	0.621 (0.005)	2.005 (0.138)	7286.222 (5773.509)	0.837 (0.031)	0.535 (0.191)	2.014 (0.424)
	cIDice	baseline	18542.667 (1171.782)	0.694 (0.016)	0.342 (0.013)	3.304 (0.243)	6167.556 (1601.572)	0.770 (0.029)	0.367 (0.054)	2.692 (0.244)
		+DA	16328.333 (1693.157)	0.661 (0.044)	0.344 (0.040)	3.595 (0.255)	5221.111 (3044.832)	0.787 (0.044)	0.414 (0.094)	2.674 (0.303)
		+DA+CoLeTra	15743.889 (592.634)	0.674 (0.025)	0.362 (0.021)	3.517 (0.035)	4159.000 (965.763)	0.804 (0.041)	0.397 (0.055)	2.650 (0.319)
	Warploss	baseline	19032.889 (1866.535)	0.683 (0.062)	0.339 (0.050)	3.420 (0.672)	22977.667 (4664.410)	0.735 (0.147)	0.450 (0.203)	2.678 (1.029)
		+DA	18922.667 (1388.622)	0.675 (0.018)	0.322 (0.015)	3.313 (0.278)	20966.111 (4222.903)	0.775 (0.066)	0.495 (0.167)	2.609 (0.644)
		+DA+CoLeTra	18698.667 (781.807)	0.662 (0.029)	0.313 (0.025)	3.532 (0.391)	24844.000 (10194.729)	0.738 (0.087)	0.465 (0.146)	2.620 (0.647)
	Topoloss	baseline	13293.333 (1556.015)	0.825 (0.011)	0.566 (0.032)	1.944 (0.107)	20388.556 (8153.324)	0.831 (0.027)	0.636 (0.038)	1.854 (0.351)
		+DA	10127.333 (1244.840)	0.848 (0.022)	0.669 (0.053)	1.874 (0.234)	24431.222 (4494.070)	0.834 (0.020)	0.701 (0.031)	1.844 (0.277)
		+DA+CoLeTra	9041.000 (682.372)	0.846 (0.010)	0.671 (0.046)	1.915 (0.146)	16779.111 (4860.278)	0.851 (0.007)	0.726 (0.010)	1.748 (0.087)

the most used loss functions for image segmentation; Dice loss, in addition, accounts for dataset imbalance. Region-Wise loss (RWLoss) [47] is a loss function that incorporates pixel importance with distance maps. cLDice [42], Warping [12], and TopoLoss [13], are topology loss functions; cLDice focuses on achieving accurate skeletons in tubular structures; Warping loss focuses on rectifying critical pixels that affect the topology of the prediction; and TopoLoss focuses on correcting topological features leveraging persistence homology. For the DRIVE, Crack500, and CREMI datasets, we trained 2D models, whereas for the Narwhal dataset we trained 3D models. For the 48 experimental scenarios, we compared models trained 1) without any data augmentation, 2) with extensive data augmentation, and 3) combining extensive data augmentation with our CoLeTra. We repeated each experiment with three random seeds to account for random sampling and initializations. Our experiments ran on a cluster with NVIDIA V100 (32GB), with each experiment taking between 1 hour and 24 hours depending on the dataset and loss function. Other details regarding the optimization can be found in Appendix B.

CoLeTra’s hyper-parameters CoLeTra has two main hyper-parameters: the number of patches (n , *i.e.*, $|C|$ in Eq. (1)) and patch size (s). These hyper-parameters, as in any data augmentation transformation, depend on the optimization task, and particularly on the dataset. Since the goal of our study was not to find the optimal values for each experimental scenario, we conducted a very simple strategy that explored only nine configurations per architecture and dataset. We optimized Cross entropy loss with patches of size 11, 15, and 19—since the structures have a similar width—and a number of patches such that, after applying CoLeTra, the maximum covered area of the structures corresponds to approximately 40%, 50%, and 60%, avoiding using too few or too many patches. The exact configurations that we explored and the configuration that yielded the best performance are detailed in Appendix C.

Metrics We measured the Dice coefficient (own implementation), the 95th percentile of Hausdorff distance (HD95)⁴, the centerline Dice (cLDice) [42], and the Betti errors. We chose these metrics since they measure different characteristics of the segmentations at the pixel, distance, and topology level. The Betti errors specifically refer to the difference in the number of connected components (Betti 0), holes (Betti 1), and cavities (Betti 2) between the predicted mask and the ground truth. These can be computed locally through several random (or sliding window) patches across the image [22], or globally in the entire image depending on whether local or global topology is more rele-

vant. Due to space limitations, here, we report the first local Betti error for DRIVE and Crack500 datasets, the second global Betti error for CREMI, and the first global Betti error for the Narwhal dataset, since these, we argue, are the most relevant for each task. All Betti errors can be found in Appendix D. Additionally, the Dice coefficient, HD95, and cLDice in CREMI dataset were measured on the axons that are the focus of the original segmentation task.

CoLeTra generally led to **smaller Betti errors** across all datasets, loss functions, and architectures, indicating higher topology accuracy (see Table 1 and Figure 4). These improvements, observed even when optimizing topology loss functions, were after applying CoLeTra on top of strong data augmentation that already increased the diversity of the training set. CoLeTra always improved TopoLoss segmentations; it improved Warping loss in every case except when optimizing AttentionUNet on the Narwhal dataset; and it improved cLDice in five out of eight dataset-architecture experimental setting combinations. When optimizing non-topology loss functions (CE, Dice, and RWLoss), CoLeTra consistently yielded topologically more accurate segmentations in DRIVE and Crack500 datasets, and in the majority of the cases in CREMI and the Narwhal dataset. Furthermore, CoLeTra achieved the smallest of all Betti errors in Crack500 and the Narwhal dataset. In CREMI dataset, the baseline appeared to yield segmentations topologically more accurate than when incorporating data augmentation since the non-data augmented baseline created more false holes (see Appendix E); in this dataset, CoLeTra improved the topology compared to using strong data augmentation. CoLeTra’s improvements were observed **consistently** across all settings, enhancing both the mean performance and reducing the large standard deviations caused by random model initializations.

CoLeTra not only reduced the Betti errors but, in many cases, it also led to better cLDice, Dice coefficients, and Hausdorff distances (see Table 1). In Crack500 dataset, the majority of the metrics improved across all loss functions and architectures. In DRIVE and the Narwhal dataset, the Betti errors consistently decreased while the other metrics fluctuated depending on the loss function and architecture. In CREMI dataset, CoLeTra improved topology accuracy without worsening the Dice coefficient and the Hausdorff distance.

4.3. Sensitivity analysis

We investigated how the two main hyper-parameters of CoLeTra—the size and number of patches—affect the topology accuracy gains. To this end, we optimized DynUNet on the DRIVE dataset with the Dice loss as described in Section 4.2. In addition to measuring the Betti error, we counted the number of small (< 30 pixels) connect components, as these structures represent fragments of bro-

⁴<http://loli.github.io/medpy/>

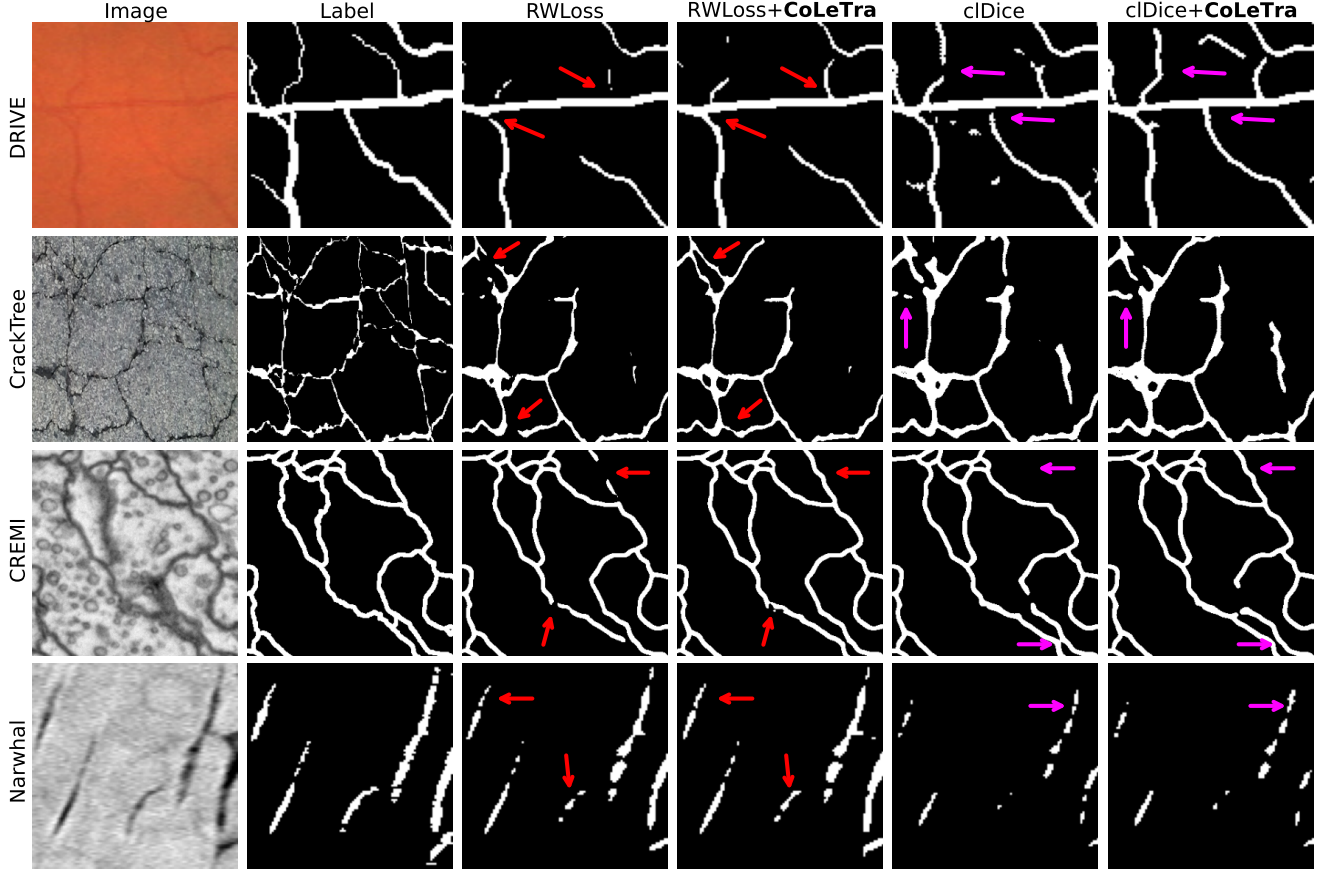


Figure 4. Example segmentations on four datasets and the best-performing loss functions, with and without CoLeTra.

ken blood vessels. With the DRIVE images containing, on average, only one or two small connected components per image, a small number of these connected components in the segmentation masks indicates high topology accuracy. We explored the number of patches $n = \{10, 20, \dots, 200\}$ and the patch sizes $s = \{3, 7, \dots, 67\}$ in two separate sets of experiments.

CoLeTra decreased the Betti error and number of small connected components with patch sizes between 10 and 120 (see Fig. 5 (a,b)). Beyond 120 patches, the Betti error and number of connected components oscillated. Similarly, the patch sizes between 3^2 and 19^2 decreased the Betti error and the number of small connected components (see Fig. 5 (c,d)). Thereafter, these metrics also started to oscillate. Figure 5 also shows that a moderately different patch size and number of patches from the ones we used in Section 4.2 ($n = 63, s = 15$) leads to similar topology accuracy.

5. Discussion

We introduced CoLeTra, a data augmentation strategy for improving topology accuracy by incorporating the prior knowledge that disconnected structures are actually con-

nected. We showed this capability on a synthetic dataset, and on four benchmark datasets with different architectures and loss functions. We also studied the sensitivity of CoLeTra to several hyper-parameter choices.

CoLeTra **consistently** led to segmentations topologically more accurate across different architectures, datasets, and loss functions. It not only reduced the Betti errors but, in many cases, CoLeTra also improved cIDice, Dice coefficient, and Hausdorff distance (see Table 1). It is important to note, however, that while improvements in non-topology metrics are a beneficial side effect, they are not the primary focus of CoLeTra. Instead, CoLeTra emphasizes topology accuracy, which is critical for downstream quantification tasks, such as counting the number of connected components. In some experimental scenarios, the performance gains were moderate, which aligns with the expected outcome of adding just one extra data augmentation transformation on top of several other data augmentations during training. A single data augmentation technique alone typically does not lead to very large performance improvements [27, 29]—even advanced strategies, such as CutOut and MixUp (see [53]).

CoLeTra demonstrates, for the first time, that **topology can be improved via data augmentation**. Although previous works have also used image inpainting to increase datasets’ diversity (see Section 2), CoLeTra is unique in that it is **specifically designed** to improve topology accuracy and it **demonstrates to do so**, even when optimizing topology loss functions (cIDice [42], Warploss [12], TopoLoss [13]). In our experiments, the loss functions that yielded the most topologically accurate segmentations across datasets and architectures were cIDice [42] and RWLoss [47], especially when applying CoLeTra, thus, aligning with contemporary work [23]. CoLeTra’s improvements demonstrate that data augmentation methods can complement topology loss functions and, potentially, deep learning architectures and postprocessing methods that focus on topology (e.g., [2, 17, 34, 52]). This capability to enhance topology accuracy alongside other methods during training is important since typical deep learning methods cannot guarantee accurate topology unless the topological features are known beforehand [4], which does not often occur.

CoLeTra’s simplicity ensures that CoLeTra is fast, while requiring no extra GPU memory. As a result, CoLeTra can be used in scenarios where other topology-enhancing methods are limited by their computational cost [12, 13, 20] or larger GPU memory requirements [42]. Additionally, CoLeTra’s simple strategy to determine where to break the tubular structures can be extended to focus on fixing specific type of breaks [35] or in other locations considered important. Exploring performance gains in particular cases was beyond the scope of our study; instead, we demonstrated that even a simple approach can improve topology accuracy.

CoLeTra has two main hyper-parameters: the size, and the number of patches that will disconnect the tubular structures. In our comparison among different architectures, datasets, and loss functions, we utilized the hyper-parameter values that we found on a very small grid search—likely a sub-optimal configuration that, nevertheless, increased the topology accuracy of the segmentations. More accurate segmentations could be achieved with a more exhaustive grid search, and by jointly accounting for the datasets’ particularities, such as the disproportion between the pixels from thin and thick structures [21], class imbalance, and noisy labels [43].

Our sensitivity analysis showed that a large number of patches and a large patch size tend to decrease the Betti error and the number of small connected components, indicating higher topology accuracy. The range of patch sizes that improved topology accuracy (from 3^2 to 23^2 , Fig. 5 (c,d)) overlaps with the range of the widths of the blood vessels (from 2 to 18.5), demonstrating that patch size can be tuned, intuitively, based on the structures’ width. Regarding the number of patches, we hypothesize that the optimal value depends on the accuracy of the annotations. In datasets with

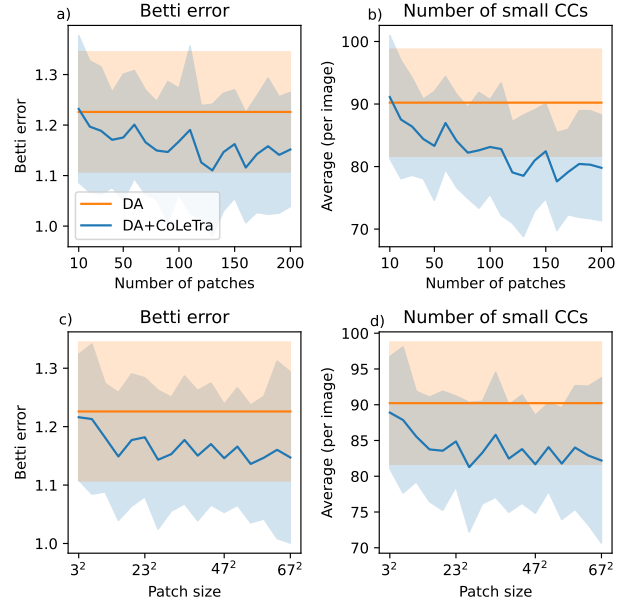


Figure 5. Betti error and number of small (< 30 pixels) connected components achieved with CoLeTra on the DRIVE dataset with different number of patches (a,b) and patch sizes (c,d). (DA—data augmentation)

noisy labels that mark visually-connected structures as disconnected (see Fig. 1 a)), the optimization will reinforce such incorrect disconnection. Since CoLeTra promotes the opposite (i.e., connecting visually-disconnected structures), a large number of patches may help compensating the structures mislabeled as disconnected.

Our experiments demonstrated that CoLeTra was beneficial on datasets with mostly accurate ground truth (DRIVE, CrackTree, CREMI) and with visually-disconnected structures that we know are connected (Narwhal dataset). However, CoLeTra’s advantageous capability of promoting the connectivity between visually-disconnected structures may be disadvantageous on structures that should not be connected. For instance, consider the validation image of our synthetic experiment (Fig. 3), where, depending on the quantification task, the connected component analysis should lead to either four lines (dashed and solid) or 14 different structures. One solution to avoid false connections is to adjust the hyper-parameter “patch size” (s in Eq. (1)).

6. Conclusion

CoLeTra increases topology accuracy in a wide range of settings, including different architectures, loss functions, and datasets. Additionally, it does not deteriorate—often, it improves—other metrics, such as Dice coefficient and Hausdorff distance. Our sensitivity analysis showed that CoLeTra is robust to different hyper-parameter choices,

and these hyper-parameters are largely intuitive, facilitating their tuning. Finally, to further encourage research in the domain of image segmentation and topology, we release the Narwhal dataset.

Acknowledgements. This work was supported by Villum Foundation and NordForsk.

References

- [1] Nick Byrne, James R Clough, Israel Valverde, Giovanni Montana, and Andrew P King. A persistent homology-based topological loss for cnn-based multiclass segmentation of cmr. *IEEE transactions on medical imaging*, 42(1):3–14, 2022. 2
- [2] Sophie Carneiro-Esteves, Antoine Vacavant, and Odysée Merveille. Restoring connectivity in vascular segmentation using a learned post-processing model. *arXiv preprint arXiv:2404.10506*, 2024. 8
- [3] Liang Chen, Paul Bentley, Kensaku Mori, Kazunari Misawa, Michitaka Fujiwara, and Daniel Rueckert. Self-supervised learning for medical image analysis using image context restoration. *Medical image analysis*, 58:101539, 2019. 3
- [4] James R Clough, Nicholas Byrne, Ilkay Oksuz, Veronika A Zimmer, Julia A Schnabel, and Andrew P King. A topological loss function for deep-learning based image segmentation using persistent homology. *IEEE transactions on pattern analysis and machine intelligence*, 44(12):8766–8778, 2020. 1, 2, 8
- [5] Edelsbrunner, Letscher, and Zomorodian. Topological persistence and simplification. *Discrete & computational geometry*, 28:511–533, 2002. 2
- [6] Rickard Br  l Gabri  lsson, Bradley J Nelson, Anjan Dwaraknath, and Primo   Skraba. A topology layer for machine learning. In *International Conference on Artificial Intelligence and Statistics*, pages 1553–1563. PMLR, 2020. 2
- [7] Allen Hatcher. *Algebraic Topology*. Cambridge University Press, 2002. 1
- [8] Hongliang He, Jun Wang, Pengxu Wei, Fan Xu, Xiangyang Ji, Chang Liu, and Jie Chen. Toposeg: Topology-aware nuclear instance segmentation. In *Proceedings of the IEEE/CVF International Conference on Computer Vision*, pages 21307–21316, 2023. 2
- [9] Kaiming He, Georgia Gkioxari, Piotr Doll  r, and Ross Girshick. Mask r-cnn. In *Proceedings of the IEEE international conference on computer vision*, pages 2961–2969, 2017. 3
- [10] Songping He, Yi Zou, Bin Li, Fangyu Peng, Xia Lu, Hui Guo, Xin Tan, and Yanyan Chen. An image inpainting-based data augmentation method for improved sclerosed glomerular identification performance with the segmentation model efficientnetb3-unet. *Scientific Reports*, 14(1):1033, 2024. 3
- [11] Christoph Hofer, Roland Kwitt, Marc Niethammer, and Andreas Uhl. Deep learning with topological signatures. *Advances in neural information processing systems*, 30, 2017. 2
- [12] Xiaoling Hu. Structure-aware image segmentation with homotopy warping. *Advances in Neural Information Processing Systems*, 35:24046–24059, 2022. 2, 6, 8
- [13] Xiaoling Hu, Fuxin Li, Dimitris Samaras, and Chao Chen. Topology-preserving deep image segmentation. *Advances in neural information processing systems*, 32, 2019. 1, 2, 6, 8
- [14] Xiaoling Hu, Dimitris Samaras, and Chao Chen. Learning probabilistic topological representations using discrete morse theory. *arXiv preprint arXiv:2206.01742*, 2022. 1, 2
- [15] Fabian Isensee, Paul F Jaeger, Simon AA Kohl, Jens Petersen, and Klaus H Maier-Hein. nnu-net: a self-configuring method for deep learning-based biomedical image segmentation. *Nature methods*, 18(2):203–211, 2021. 5
- [16] Umair Javaid, Damien Dasnoy, and John A Lee. Semantic segmentation of computed tomography for radiotherapy with deep learning: compensating insufficient annotation quality using contour augmentation. In *Medical Imaging 2019: Image Processing*, pages 682–694. SPIE, 2019. 2
- [17] Qiangguo Jin, Zhaopeng Meng, Tuan D Pham, Qi Chen, Leyi Wei, and Ran Su. Dunet: A deformable network for retinal vessel segmentation. *Knowledge-Based Systems*, 178: 149–162, 2019. 8
- [18] Yannick Kirchhoff, Maximilian R Rokuss, Saikat Roy, Balint Kovacs, Constantin Ulrich, Tassilo Wald, Maximilian Zenk, Philipp Vollmuth, Jens Kleesiek, Fabian Isensee, et al. Skeleton recall loss for connectivity conserving and resource efficient segmentation of thin tubular structures. In *European Conference on Computer Vision*, pages 218–234. Springer, 2024. 2
- [19] Junjie Li, Zilei Wang, and Xiaoming Hu. Learning intact features by erasing-inpainting for few-shot classification. In *Proceedings of the AAAI Conference on Artificial Intelligence*, pages 8401–8409, 2021. 3
- [20] Wei Liao. Segmentation of tubular structures using iterative training with tailored samples. In *Proceedings of the IEEE/CVF International Conference on Computer Vision*, pages 23643–23652, 2023. 1, 2, 8
- [21] Jun Hao Liew, Scott Cohen, Brian Price, Long Mai, and Jia-shi Feng. Deep interactive thin object selection. In *Proceedings of the IEEE/CVF Winter Conference on Applications of Computer Vision*, pages 305–314, 2021. 8
- [22] Manxi Lin, Kilian Zepf, Anders Nymark Christensen, Zahra Bashir, Morten Bo S  ndergaard Svendsen, Martin Tolsgaard, and Aasa Feragen. Dtu-net: learning topological similarity for curvilinear structure segmentation. In *International Conference on Information Processing in Medical Imaging*, pages 654–666. Springer, 2023. 6
- [23] Chuni Liu, Boyuan Ma, Xiaojuan Ban, Yujie Xie, Hao Wang, Weihua Xue, Jingchao Ma, and Ke Xu. Enhancing boundary segmentation for topological accuracy with skeleton-based methods. *arXiv preprint arXiv:2404.18539*, 2024. 8
- [24] Cl  ment Maria, Jean-Daniel Boissonnat, Marc Glisse, and Mariette Yvinec. The gudhi library: Simplicial complexes and persistent homology. In *Mathematical Software–ICMS 2014: 4th International Congress, Seoul, South Korea, August 5-9, 2014. Proceedings 4*, pages 167–174. Springer, 2014. 2, 14

- [25] Fausto Milletari, Nassir Navab, and Seyed-Ahmad Ahmadi. V-net: Fully convolutional neural networks for volumetric medical image segmentation. In *2016 fourth international conference on 3D vision (3DV)*, pages 565–571. Ieee, 2016. 5
- [26] Shervin Minaee, Yuri Boykov, Fatih Porikli, Antonio Plaza, Nasser Kehtarnavaz, and Demetri Terzopoulos. Image segmentation using deep learning: A survey. *IEEE transactions on pattern analysis and machine intelligence*, 44(7):3523–3542, 2021. 1
- [27] Alhassan Mumuni and Fuseini Mumuni. Data augmentation: A comprehensive survey of modern approaches. *Array*, 16: 100258, 2022. 7
- [28] Andriy Myronenko. 3d mri brain tumor segmentation using autoencoder regularization. In *Brainlesion: Glioma, Multiple Sclerosis, Stroke and Traumatic Brain Injuries: 4th International Workshop, BrainLes 2018, Held in Conjunction with MICCAI 2018, Granada, Spain, September 16, 2018, Revised Selected Papers, Part II 4*, pages 311–320. Springer, 2019. 2
- [29] Loris Nanni, Michelangelo Paci, Sheryl Brahnam, and Alessandra Lumini. Comparison of different image data augmentation approaches. *Journal of imaging*, 7(12):254, 2021. 7
- [30] Yunhao Nie, Bo Lu, Qiyuan Chen, Qinghai Miao, and Yisheng Lv. Synposes: Generating virtual dataset for pedestrian detection in corner cases. *IEEE Journal of Radio Frequency Identification*, 6:801–804, 2022. 3
- [31] Ozan Oktay, Jo Schlemper, Loic Le Folgoc, Matthew Lee, Mattias Heinrich, Kazunari Misawa, Kensaku Mori, Steven McDonagh, Nils Y Hammerla, Bernhard Kainz, et al. Attention u-net: Learning where to look for the pancreas. *arxiv preprint arXiv:1804.03999*, 1804. 5
- [32] Doruk Oner, Adélie Garin, Mateusz Koziński, Kathryn Hess, and Pascal Fua. Persistent homology with improved locality information for more effective delineation. *IEEE Transactions on Pattern Analysis and Machine Intelligence*, 2023. 2
- [33] Deepak Pathak, Philipp Krahenbuhl, Jeff Donahue, Trevor Darrell, and Alexei A Efros. Context encoders: Feature learning by inpainting. In *Proceedings of the IEEE conference on computer vision and pattern recognition*, pages 2536–2544, 2016. 3
- [34] Yaolei Qi, Yuting He, Xiaoming Qi, Yuan Zhang, and Guanyu Yang. Dynamic snake convolution based on topological geometric constraints for tubular structure segmentation. In *Proceedings of the IEEE/CVF International Conference on Computer Vision*, pages 6070–6079, 2023. 8
- [35] Jiaxiang Ren, Zhenghong Li, Wensheng Cheng, Zhilin Zou, Kicheon Park, Yingtian Pan, and Haibin Ling. Self-supervised 3d skeleton completion for vascular structures. In *International Conference on Medical Image Computing and Computer-Assisted Intervention*, pages 579–589. Springer, 2024. 8
- [36] Daniel V Ruiz, Bruno A Krinski, and Eduardo Todt. Anda: A novel data augmentation technique applied to salient object detection. In *2019 19th International Conference on Advanced Robotics (ICAR)*, pages 487–492. IEEE, 2019. 3
- [37] Daniel V Ruiz, Bruno A Krinski, and Eduardo Todt. Ida: Improved data augmentation applied to salient object detection. In *2020 33rd SIBGRAPI Conference on Graphics, Patterns and Images (SIBGRAPI)*, pages 210–217. IEEE, 2020. 3
- [38] Plabon Kumar Saha, Sinthia Ahmed, Tajbiul Ahmed, Hasidul Islam, Al Imran, AZM Tahmidul Kabir, et al. Data augmentation technique to expand road dataset using mask rcnn and image inpainting. In *2021 International Conference on Intelligent Technologies (CONIT)*, pages 1–6. IEEE, 2021. 3
- [39] Jialin Shi, Kailai Zhang, Chenyi Guo, Youquan Yang, Yali Xu, and Ji Wu. A survey of label-noise deep learning for medical image analysis. *Medical Image Analysis*, 95: 103166, 2024. 2
- [40] Pengcheng Shi, Jiesi Hu, Yanwu Yang, Zilve Gao, Wei Liu, and Ting Ma. Centerline boundary dice loss for vascular segmentation. In *International Conference on Medical Image Computing and Computer-Assisted Intervention*, pages 46–56. Springer, 2024. 2
- [41] Seung Yeon Shin, Sungwon Lee, Daniel Elton, James L Gulley, and Ronald M Summers. Deep small bowel segmentation with cylindrical topological constraints. In *Medical Image Computing and Computer Assisted Intervention—MICCAI 2020: 23rd International Conference, Lima, Peru, October 4–8, 2020, Proceedings, Part IV 23*, pages 207–215. Springer, 2020. 2
- [42] Suprosanna Shit, Johannes C Paetzold, Anjany Sekuboyina, Ivan Ezhov, Alexander Unger, Andrey Zhyhka, Josien PW Pluim, Ulrich Bauer, and Bjoern H Menze. clDice—a novel topology-preserving loss function for tubular structure segmentation. In *Proceedings of the IEEE/CVF conference on computer vision and pattern recognition*, pages 16560–16569, 2021. 1, 2, 6, 8
- [43] Hwanjun Song, Minseok Kim, Dongmin Park, Yooju Shin, and Jae-Gil Lee. Learning from noisy labels with deep neural networks: A survey. *IEEE transactions on neural networks and learning systems*, 2022. 8
- [44] Joes Staal, Michael D Abràmoff, Meindert Niemeijer, Max A Viergever, and Bram Van Ginneken. Ridge-based vessel segmentation in color images of the retina. *IEEE transactions on medical imaging*, 23(4):501–509, 2004. 4
- [45] Roman Suvorov, Elizaveta Logacheva, Anton Mashikhin, Anastasia Remizova, Arsenii Ashukha, Aleksei Silvestrov, Naejin Kong, Harshith Goka, Kiwoong Park, and Victor Lempitsky. Resolution-robust large mask inpainting with fourier convolutions. In *Proceedings of the IEEE/CVF winter conference on applications of computer vision*, pages 2149–2159, 2022. 3
- [46] Takeshi Teshima and Masashi Sugiyama. Incorporating causal graphical prior knowledge into predictive modeling via simple data augmentation. In *Uncertainty in Artificial Intelligence*, pages 86–96. PMLR, 2021. 2
- [47] Juan Miguel Valverde and Jussi Tohka. Region-wise loss for biomedical image segmentation. *Pattern Recognition*, 136: 109208, 2023. 6, 8
- [48] Shiyao Wang, Qi Liu, Yicheng Zhong, Zhilong Zhou, Tiezheng Ge, Defu Lian, and Yuning Jiang. Creagan: An

- automatic creative generation framework for display advertising. In *Proceedings of the 30th ACM International Conference on Multimedia*, pages 7261–7269, 2022. [3](#)
- [49] Nina Kølln Wittig, Maja Østergaard, Jonas Palle, Thorbjørn Erik Køppen Christensen, Bente Lomholt Langdahl, Lars Rejnmark, Ellen-Margrethe Hauge, Annemarie Brüel, Jesper Skovhus Thomsen, and Henrik Birkedal. Opportunities for biomineralization research using multiscale computed x-ray tomography as exemplified by bone imaging. *Journal of Structural Biology*, 214(1):107822, 2022. [12](#)
- [50] Benyi Yang, Zhenyu Liu, Guifang Duan, and Jianrong Tan. Mask2defect: A prior knowledge-based data augmentation method for metal surface defect inspection. *IEEE Transactions on Industrial Informatics*, 18(10):6743–6755, 2021. [2](#)
- [51] Fan Yang, Lei Zhang, Sijia Yu, Danil Prokhorov, Xue Mei, and Haibin Ling. Feature pyramid and hierarchical boosting network for pavement crack detection. *IEEE Transactions on Intelligent Transportation Systems*, 21(4):1525–1535, 2019. [4](#)
- [52] Xin Yang, Zhiqiang Li, Yingqing Guo, and Dake Zhou. Dcu-net: A deformable convolutional neural network based on cascade u-net for retinal vessel segmentation. *Multimedia Tools and Applications*, 81(11):15593–15607, 2022. [8](#)
- [53] Sangdoo Yun, Dongyoon Han, Seong Joon Oh, Sanghyuk Chun, Junsuk Choe, and Youngjoon Yoo. Cutmix: Regularization strategy to train strong classifiers with localizable features. In *Proceedings of the IEEE/CVF international conference on computer vision*, pages 6023–6032, 2019. [7](#)
- [54] I Zanette, B Enders, M Dierolf, P Thibault, Regine Gradl, Ana Diaz, Manuel Guizar-Sicairos, A Menzel, Franz Pfeiffer, and Paul Zaslansky. Ptychographic x-ray nanotomography quantifies mineral distributions in human dentine. *Scientific Reports*, 5(1):9210, 2015. [12](#)
- [55] Lingzhi Zhang, Tarmily Wen, Jie Min, Jiancong Wang, David Han, and Jianbo Shi. Learning object placement by inpainting for compositional data augmentation. In *Computer Vision—ECCV 2020: 16th European Conference, Glasgow, UK, August 23–28, 2020, Proceedings, Part XIII 16*, pages 566–581. Springer, 2020. [3](#)
- [56] Zhun Zhong, Liang Zheng, Guoliang Kang, Shaozi Li, and Yi Yang. Random erasing data augmentation. In *Proceedings of the AAAI conference on artificial intelligence*, pages 13001–13008, 2020. [3](#)

Disconnect to Connect: A Data Augmentation Method for Improving Topology Accuracy in Image Segmentation

Supplementary Material

A. The Narwhal dataset

A.1. Image acquisition and reconstruction

Narwhal tusks, composed of an inner dentine ring with pores (dentine tubules) running through it [54], can be effectively studied using microcomputed tomography, particularly synchrotron radiation microcomputed tomography (SR- μ CT) [49]. In order to study its internal structure, a piece of narwhal tusk was cut radially, with respect to the tusk length, to a square rod with side lengths $460\text{ }\mu\text{m}$ by $530\text{ }\mu\text{m}$ using a diamond blade saw (Accutom-5, Struers, Ballerup, Denmark). The rod was imaged with SR- μ CT in the Paul Scherrer Institute, Viligen, Switzerland, at the TOMCAT beamline X02DA of the Swiss Light Source. Several scans were measured along the long axis of the rod to image it entirely. For each scan, 2000 projections were collected covering 180° with an energy of 18 keV, and an exposure time of 150 ms. 30 closed beam images were used for dark field correction and 50 open beam images for flat field correction. A $20\text{ }\mu\text{m}$ LuAG:Ce scintillator, a microscope (Optique Peter, France) with a $\times 20$ magnification and a PCO.Edge 5.5 camera (PCO AG, Kelheim, Germany) gave rise to an isotropic voxel size of $0.325\text{ }\mu\text{m}$.

Image reconstruction was performed on-site using the GridRec algorithm in the RecoManagerRa pipeline plug-in for ImageJ. In the reconstruction, a Parzen filter with a cut-off frequency of 0.5 was employed as well as standard ring removal. The data was scaled to be between -4×10^{-4} and 8×10^{-4} , and output as 16-bit grey level images. Each scan had dimensions of $2560 \times 2560 \times 2160$ voxels.

A.2. Training, validation, and test splits

For the purpose of this study, we employed five scans containing abundant dentine tubules. One scan, used for training, was divided into 64 overlapping patches. Then, we discarded those patches containing background area, leading to our training set of 20 patches of, approximately, $591 \times 530 \times 583$ voxels. The validation set corresponds to a $500 \times 500 \times 500$ patch from another scan, and the test set is comprised by three $500 \times 500 \times 500$ patches, each from a different scan.

A.3. Labels

Due to the extremely large size of the images, making their manual annotation prohibitively expensive, we derived pseudo-labels for the training set and pseudo-ground truths for the validation and test set. The pseudo-labels were ob-

tained via thresholding to simulate the common practice employed by researchers when analyzing these type of images. The pseudo-ground truths, used exclusively to evaluate the predictions, were derived through a more elaborated process yielding segmentation masks that, although they were not perfect, they permit measuring topology accuracy reliably (i.e., counting the number of tubules), and permit quantifying tubules' properties, such as their directionality.

Pseudo-labels (training set) First, we thresholded the images and considered as “dentine tubule” those voxels with intensities below 17,450—threshold that we found experimentally. Then, we removed non-tubular areas that we identified with a distance transform.

Pseudo-ground truth (validation and test set) The pseudo-ground truth labels are created by first tracking the tubules through the volume and then assigning labels to the tracks. In unmineralized regions of the tusk, the intensity of the tubule and the regions are the same, which makes segmentation challenging. By utilizing that the dentine tubules are running predominantly along the z -direction of the volume, we can track the tubules to obtain their center lines.

Tracking is done by initially detecting the tubule's center position and connecting detected points moving along the z -direction. The center position is detected as the local maxima in a Gaussian-smoothed image ($\sigma = 1.5$). We connect mutually closest points in consecutive frames under some constraints. Points in one frame must be separated by an Euclidean distance of at least five voxels, be within an Euclidean distance of no more than three voxels in consecutive frames, if no points are detected within five frames tracks are stopped, and we only keep tracks that are at least 20 voxels long (Euclidean distance). Based on the tracks, we create a label image containing a thresholded version of the original image (threshold value of 30,720) but masked along the tracks. We employ a minimum mask of a 3×3 window that the label should minimally be, and a maximum mask of a circle with a diameter of 5×5 that the label can maximally obtain. If the thresholded image is within these limits, the threshold will be chosen. After labeling, we see tubules being tracked nicely through the unmineralized regions, and labels that connect in a complex network as you will expect for dentine tubules. Tracks are illustrated in Fig. 6.

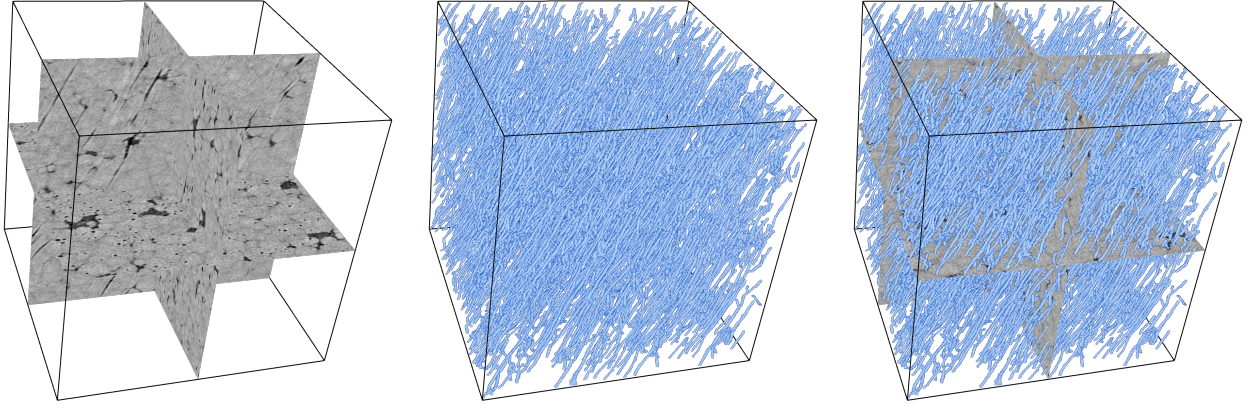


Figure 6. Example of labels in the Narwhal Dataset. Left shows orthogonal central slices from the volume, middle shows the labels, and right shows the two together.

A.4. Dataset availability

The Narwhal dataset, released under CC BY-NC 4.0 licence, can be downloaded at https://archive.compute.dtu.dk/files/public/projects/CoLeTra_Narwhal.

B. Optimization

B.1. Architectures

We optimized two model architectures: DynUNet⁵ and AttentionUNet⁶.

DynUNet had the same architecture in all our experiments, differing only in the dimension of the kernels and the input channels. In DRIVE, Crack500, and CREMI datasets we used 2D kernels (*spatial_dims* = 2), and in the Narwhal dataset we used 3D kernels (*spatial_dims* = 3). DRIVE and Crack500 contained RGB images (*in_channels* = 3) whereas CREMI and the Narwhal dataset contained single-channel images (*in_channels* = 1). DynUNet had four downsampling blocks that used convolutions with strides = 2 to reduce the dimensionality of the features. Additionally, DynUNet employed deep supervision, optimizing the output of three upsampling blocks. The exact configuration of DynUNet was:

```
DynUNet(spatial_dims, in_channels,
        out_channels=2,
        kernel_size=[3, 3, 3, 3, 3, 3],
        strides=[1, 2, 2, 2, 2, 2],
        upsample_kernel_size=[2, 2, 2, 2, 2],
```

```
        deep_supervision=True,
        deep_supr_num=3)
```

AttentionUNet architecture differed across datasets. We initially aimed to configure AttentionUNet to match, as much as possible, the number of parameters of DynUNet. However, due to the larger GPU memory requirements, we used a smaller and shallower architecture in some datasets. The dimension of the kernels and the input channels were as in DynUNet. Additionally, the depth and the number of feature maps per block were as follows:

DRIVE and Crack500

```
AttentionUNet(spatial_dims=2,
              in_channels=3, out_channels=2,
              channels=[32, 64, 128, 256, 512, 512],
              strides=[1, 2, 2, 2, 2, 2])
```

CREMI

```
AttentionUNet(spatial_dims=2,
              in_channels=1, out_channels=2,
              channels=[16, 32, 64, 128],
              strides=[1, 2, 2, 2])
```

Narwhal

```
AttentionUNet(spatial_dims=3,
              in_channels=1, out_channels=2,
              channels=[16, 24, 32],
              strides=[1, 2, 2])
```

B.2. Data augmentation and sampling strategy

All images were randomly augmented, with a 50% probability in each transform independently, with random Gaussian noise ($\mu = 0, \sigma = 1$), random gamma correction

⁵<https://docs.monai.io/en/stable/networks.html#dynunet>

⁶<https://docs.monai.io/en/stable/networks.html#attentionunet>

($\gamma \in [0.8, 1.2]$), and random axis flip. DRIVE images were, in addition, randomly re-scaled between $[1, 1.75]$. Since CREMI and Narwhal images were too big to fit the GPU memory, we sampled, after applying the Gaussian noise, 15 slices in CREMI dataset and $15 \times 128 \times 128 \times 128$ patches in the Narwhal dataset. We sampled only 15 slices/patches to ensure diversity in the data augmentation; note that we optimized the models for a certain number of iterations and not epochs.

B.3. Optimization

We utilized Adam optimizer with a starting learning rate of 0.001 and weight decay of 10^{-5} . We decreased the learning rate during training: $\eta \leftarrow \eta(1 - \frac{iteration}{max.iterations})^{0.9}$. For DRIVE, Crack500, CREMI, and the Narwhal dataset, we optimized the models for 5000, 7000, 4000, 1000 iterations, respectively. In addition, due to the class imbalance in the Narwhal dataset, we used weighted Cross entropy (including in TopoLoss that relies on Cross entropy) with the following weights: $[0.05, 0.95]$. The rectified region wise maps employed by RWLoss in the Narwhal dataset were also multiplied by those weights accordingly.

C. CoLeTra’s hyper-parameters search

For each dataset and architecture, we explored a maximum of nine different configurations combining three patch sizes (s) and three number of patches (n). For the patch sizes, we explored the values 11, 15, and 19 since the structures to be segmented have a width around that range. For the number of patches, to avoid disconnecting too many or too few structures, we designed a simple strategy based on the number of pixels in the annotated areas. Given the average number of pixels and a patch size, consider the number of patches such that the maximum covered area of the structures after applying CoLeTra corresponds to approximately 40%, 50%, and 60% of the total.

In the tables below, we specified exactly which combination of hyper-parameters were explored, and which one yielded the best performance in DynUNet (D) and AttentionUNet (A) architectures. Note that, in the Narwhal dataset, a single patch size of $15 \times 15 \times 15$ and $19 \times 19 \times 19$ already covers more than the expected number voxels from the structure to be found in the $128 \times 128 \times 128$ patches used during training. Thus, we only explored to apply a single patch when its size was 15 or 19.

D. Betti Errors

Tables 6 and 7 show all the Betti errors (global and local) obtained in our experiments, which were computed via the Gudhi library [24]. The global Betti errors were the difference in the Betti numbers between the entire ground-truth annotation and the prediction. The local Betti er-

s	n	$\checkmark?$
11	94	
11	117	
11	141	
15	50	
15	63	D
15	75	
19	31	
19	39	A
19	47	

Table 2. DRIVE

s	n	$\checkmark?$
11	819	
11	1024	
11	1229	
15	440	
15	551	
15	661	
19	274	A
19	343	D
19	412	

Table 4. CREMI

s	n	$\checkmark?$
11	57	
11	71	
11	86	
15	30	A
15	38	
15	46	
19	19	D
19	24	
19	28	

Table 3. Crack500

s	n	$\checkmark?$
11	2	D
11	3	
11	4	
15	1	A
19	1	

Table 5. Narwhal

rors were computed similarly but in patches of size 64×64 patches (2D images) or $48 \times 48 \times 48$ (3D images). The patches were extracted either randomly or in a sliding-window manner depending on whether the total number of non-overlapping patches that could be extracted from the images were more than 500 (for 2D images) or 100 (for 3D images).

E. Holes in CREMI segmentations

The Betti 1 number in CREMI dataset refers to the number of holes in the segmentations. This number roughly corresponds to the number of axons in the image, hence its importance. Two segmentations with a similar number of holes—regardless of whether the holes were accurately located—will have a low Betti 1 error. In CREMI dataset, we observe that the baselines (without any data augmentation) produced more holes that are incorrect than models trained with data augmentation and CoLeTra. Thus, baselines, despite achieving smaller Betti 1 errors, yielded worse segmentations than when applying data augmentation and CoLeTra. Figure 7 illustrates this.

			Betti 0 (local)	Betti 1 (local)	Betti 0 (global)	Betti 1 (global)	Betti 2 (local)	Betti 2 (global)
DRIVE	CE	baseline	3.687 (0.581)	0.466 (0.080)	337.667 (51.307)	17.167 (8.807)	-	-
		+DA	1.334 (0.128)	0.233 (0.019)	114.150 (11.780)	35.467 (2.423)	-	-
		+DA+CoLeTra	1.282 (0.109)	0.241 (0.022)	108.633 (10.248)	33.550 (2.879)	-	-
	Dice	baseline	3.952 (0.345)	0.555 (0.076)	358.483 (30.392)	22.333 (7.793)	-	-
		+DA	1.226 (0.119)	0.239 (0.026)	101.183 (10.821)	28.500 (3.314)	-	-
		+DA+CoLeTra	1.149 (0.110)	0.245 (0.023)	93.200 (9.244)	26.217 (3.631)	-	-
	RWLoss	baseline	3.224 (0.531)	0.492 (0.113)	294.067 (47.585)	19.100 (11.038)	-	-
		+DA	0.992 (0.075)	0.230 (0.021)	77.050 (8.219)	29.133 (2.809)	-	-
		+DA+CoLeTra	0.984 (0.076)	0.232 (0.026)	73.800 (6.248)	28.167 (3.095)	-	-
	cIDice	baseline	3.597 (0.469)	0.462 (0.085)	322.133 (43.438)	18.017 (8.760)	-	-
		+DA	0.747 (0.084)	0.244 (0.030)	42.817 (7.331)	23.950 (3.162)	-	-
		+DA+CoLeTra	0.741 (0.084)	0.246 (0.033)	41.633 (6.619)	22.100 (3.395)	-	-
Crack500	WarpLoss	baseline	3.982 (0.413)	0.508 (0.064)	360.317 (38.095)	19.000 (6.011)	-	-
		+DA	1.211 (0.105)	0.242 (0.028)	99.233 (9.200)	27.967 (3.772)	-	-
		+DA+CoLeTra	1.166 (0.103)	0.242 (0.031)	94.533 (10.018)	25.733 (2.785)	-	-
	TopoLoss	baseline	3.631 (0.494)	0.466 (0.075)	334.017 (43.324)	16.100 (7.402)	-	-
		+DA	1.310 (0.132)	0.239 (0.018)	111.183 (13.370)	34.983 (2.287)	-	-
		+DA+CoLeTra	1.291 (0.108)	0.241 (0.026)	110.433 (11.320)	33.617 (2.820)	-	-
	CE	baseline	0.187 (0.028)	0.030 (0.008)	16.127 (4.156)	3.183 (1.079)	-	-
		+DA	0.136 (0.019)	0.031 (0.011)	9.687 (2.613)	3.210 (1.489)	-	-
		+DA+CoLeTra	0.132 (0.017)	0.029 (0.008)	9.135 (2.385)	2.943 (1.103)	-	-
	Dice	baseline	0.179 (0.027)	0.026 (0.006)	16.562 (4.249)	2.973 (0.924)	-	-
		+DA	0.125 (0.014)	0.023 (0.003)	9.422 (1.860)	2.648 (0.453)	-	-
		+DA+CoLeTra	0.124 (0.012)	0.022 (0.003)	9.458 (1.662)	2.642 (0.488)	-	-
CREMI	RWLoss	baseline	0.164 (0.025)	0.023 (0.004)	13.900 (3.586)	2.957 (0.607)	-	-
		+DA	0.125 (0.012)	0.021 (0.002)	9.313 (1.785)	2.770 (0.376)	-	-
		+DA+CoLeTra	0.122 (0.013)	0.021 (0.002)	9.177 (1.581)	2.773 (0.345)	-	-
	cIDice	baseline	0.136 (0.016)	0.023 (0.005)	10.307 (2.054)	2.733 (0.725)	-	-
		+DA	0.126 (0.014)	0.378 (0.338)	10.337 (0.959)	54.492 (49.838)	-	-
		+DA+CoLeTra	0.128 (0.011)	0.667 (0.306)	10.522 (0.886)	96.082 (44.202)	-	-
	WarpLoss	baseline	0.180 (0.029)	0.026 (0.006)	16.843 (4.035)	2.938 (0.860)	-	-
		+DA	0.125 (0.013)	0.023 (0.003)	9.573 (1.757)	2.655 (0.525)	-	-
		+DA+CoLeTra	0.124 (0.012)	0.022 (0.003)	9.535 (1.694)	2.608 (0.454)	-	-
	TopoLoss	baseline	0.189 (0.032)	0.028 (0.007)	16.352 (4.455)	3.140 (1.031)	-	-
		+DA	0.135 (0.018)	0.031 (0.011)	9.653 (2.351)	3.200 (1.418)	-	-
		+DA+CoLeTra	0.133 (0.018)	0.029 (0.010)	9.288 (2.357)	2.957 (1.277)	-	-
Nurwhal	CE	baseline	10.991 (1.669)	30.014 (4.704)	1957.333 (336.807)	32995.333 (906.375)	6.328 (1.072)	721.667 (203.312)
		+DA	7.359 (0.565)	22.289 (1.044)	1369.333 (105.285)	37514.333 (470.435)	7.289 (1.183)	853.778 (85.000)
		+DA+CoLeTra	7.966 (0.451)	22.874 (1.390)	1394.556 (71.765)	36150.444 (864.843)	7.524 (1.110)	914.333 (81.761)
	Dice	baseline	15.706 (0.994)	28.856 (2.523)	3282.000 (283.227)	31676.556 (471.876)	5.503 (0.742)	639.111 (67.779)
		+DA	5.448 (0.274)	22.841 (1.166)	103.000 (59.941)	38809.111 (888.314)	7.174 (1.015)	776.556 (60.350)
		+DA+CoLeTra	6.430 (0.478)	21.429 (1.322)	1179.444 (58.234)	37319.333 (919.677)	7.417 (1.004)	866.111 (66.730)
	RWLoss	baseline	13.958 (1.534)	27.563 (3.052)	2805.778 (317.156)	33455.111 (909.125)	5.528 (0.795)	706.000 (140.352)
		+DA	5.559 (0.296)	22.180 (1.249)	991.556 (66.776)	38493.000 (843.885)	7.043 (0.949)	739.333 (93.217)
		+DA+CoLeTra	6.448 (0.438)	21.326 (1.810)	1080.778 (49.416)	36568.889 (1473.720)	7.381 (1.118)	867.222 (52.390)
	cIDice	baseline	11.519 (0.700)	27.849 (2.191)	2185.556 (170.977)	33945.444 (770.907)	6.377 (1.054)	679.556 (92.140)
		+DA	4.117 (0.305)	24.598 (2.480)	447.556 (24.194)	41323.889 (1194.337)	7.519 (1.046)	890.111 (26.636)
		+DA+CoLeTra	4.147 (0.370)	24.634 (1.910)	454.333 (36.057)	40092.667 (632.833)	7.521 (1.172)	935.222 (32.975)
Nurwhal	WarpLoss	baseline	15.899 (1.134)	30.491 (2.222)	3344.444 (278.889)	31639.889 (588.069)	5.411 (0.699)	630.222 (56.870)
		+DA	5.366 (0.295)	22.832 (1.640)	973.000 (51.410)	38704.667 (921.115)	7.211 (1.012)	791.889 (48.693)
		+DA+CoLeTra	6.439 (0.218)	20.963 (0.736)	1108.667 (67.111)	37300.000 (886.955)	7.436 (1.004)	879.889 (48.990)
	TopoLoss	baseline	10.747 (1.549)	29.631 (3.547)	1897.778 (283.742)	32699.667 (728.942)	6.157 (0.936)	685.778 (160.521)
		+DA	7.229 (0.780)	22.991 (0.438)	1351.667 (198.445)	37760.444 (986.411)	7.346 (1.152)	840.556 (64.408)
		+DA+CoLeTra	8.100 (0.542)	23.248 (1.219)	1403.444 (76.766)	36387.444 (1036.850)	7.517 (1.107)	928.000 (93.275)
	CE	baseline	74.893 (5.746)	5.671 (0.937)	12805.889 (787.121)	501.778 (384.715)	0.387 (0.102)	35.444 (18.077)
		+DA	56.417 (6.882)	5.098 (0.995)	9907.778 (1128.195)	336.000 (367.853)	0.428 (0.189)	45.000 (16.904)
		+DA+CoLeTra	50.440 (3.140)	5.896 (1.855)	8988.556 (429.358)	665.444 (288.511)	0.359 (0.084)	36.333 (14.139)
	Dice	baseline	117.654 (13.725)	6.852 (0.252)	20779.889 (1659.472)	1065.667 (29.020)	0.316 (0.059)	51.667 (0.000)
		+DA	112.273 (3.755)	7.084 (0.343)	20280.111 (249.327)	1105.333 (25.464)	0.316 (0.059)	51.556 (0.192)
		+DA+CoLeTra	100.478 (7.622)	7.051 (0.274)	18457.111 (1220.830)	1103.000 (33.717)	0.316 (0.059)	51.667 (0.000)
Nurwhal	RWLoss	baseline	118.226 (34.077)	4.414 (0.596)	20010.444 (5278.833)	311.111 (180.449)	0.314 (0.057)	51.222 (0.770)
		+DA	73.481 (17.021)	5.548 (0.370)	12697.000 (2712.586)	806.000 (30.818)	0.316 (0.059)	51.556 (0.192)
		+DA+CoLeTra	76.217 (19.704)	5.382 (0.855)	13046.778 (3102.622)	707.556 (206.728)	0.316 (0.060)	51.444 (0.385)
	cIDice	baseline	102.843 (7.296)	7.080 (0.399)	18542.667 (1171.782)	1102.556 (24.220)	0.316 (0.059)	51.667 (0.000)
		+DA	87.116 (9.809)	7.316 (0.278)	16328.333 (1693.157)	1146.667 (6.080)	0.316 (0.059)	51.667 (0.000)
		+DA+CoLeTra	84.171 (2.495)	7.278 (0.393)	15743.889 (592.634)	1139.333 (12.409)	0.316 (0.059)	51.667 (0.000)
	WarpLoss	baseline	105.943 (15.098)	6.983 (0.367)	19032.889 (1866.535)	1080.556 (35.777)	0.316 (0.059)	51.667 (0.000)
		+DA	103.824 (9.256)	7.091 (0.334)	18922.667 (1388.622)	1103.667 (25.921)	0.316 (0.059)	51.667 (0.000)
		+DA+CoLeTra	102.377 (4.643)	7.061 (0.259)	18698.667 (781.807)	1103.111 (35.317)	0.316 (0.059)	51.667 (0.000)
	TopoLoss	baseline	77.483 (11.234)	6.051 (1.860)	13293.333 (1556.015)	578.556 (413.398)	0.329 (0.071)	43.444 (5.701)
		+DA	57.346 (8.059)	5.336 (1.082)	10127.333 (1244.840)	416.111 (240.523)	0.573 (0.447)	70.444 (45.384)
		+DA+CoLeTra	50.543 (6.165)	5.010 (1.332)	9041.000 (682.372)	414.333 (232.380)	0.400 (0.176)	33.111 (23.333)

Table 6. Betti Errors (DynUNet)

			Betti 0 (local)	Betti 1 (local)	Betti 0 (global)	Betti 1 (global)	Betti 2 (local)	Betti 2 (global)
DRIVE	CE	baseline	3.925 (0.431)	0.553 (0.132)	348.067 (40.037)	23.500 (12.783)	-	-
		+DA	1.421 (0.149)	0.241 (0.023)	121.017 (13.575)	34.867 (3.057)	-	-
		+DA+CoLeTra	1.390 (0.155)	0.241 (0.024)	118.900 (13.706)	32.217 (2.762)	-	-
	Dice	baseline	2.619 (0.462)	0.366 (0.076)	229.183 (43.137)	16.733 (7.615)	-	-
		+DA	0.974 (0.189)	0.235 (0.021)	75.533 (19.368)	29.183 (3.362)	-	-
		+DA+CoLeTra	0.930 (0.156)	0.240 (0.027)	69.433 (16.682)	27.750 (3.358)	-	-
	RWLoss	baseline	2.758 (0.378)	0.382 (0.068)	243.050 (30.951)	17.567 (9.296)	-	-
		+DA	0.815 (0.119)	0.240 (0.025)	58.717 (11.679)	29.933 (3.095)	-	-
		+DA+CoLeTra	0.806 (0.100)	0.240 (0.028)	56.817 (11.216)	29.933 (3.049)	-	-
	cDice	baseline	1.889 (0.261)	0.407 (0.152)	155.800 (23.731)	20.833 (13.767)	-	-
		+DA	0.657 (0.068)	0.254 (0.048)	34.700 (5.214)	19.567 (4.870)	-	-
		+DA+CoLeTra	0.664 (0.083)	0.248 (0.032)	34.333 (5.368)	19.117 (3.329)	-	-
Cruc500	Warploss	baseline	2.592 (0.454)	0.360 (0.071)	226.467 (42.879)	16.900 (6.966)	-	-
		+DA	0.974 (0.189)	0.235 (0.021)	75.533 (19.368)	29.183 (3.362)	-	-
		+DA+CoLeTra	0.937 (0.159)	0.234 (0.022)	70.167 (16.597)	28.033 (2.961)	-	-
	TopoLoss	baseline	4.151 (0.512)	0.576 (0.144)	370.650 (45.387)	24.683 (15.218)	-	-
		+DA	1.421 (0.149)	0.241 (0.023)	121.017 (13.575)	34.867 (3.057)	-	-
		+DA+CoLeTra	1.412 (0.157)	0.240 (0.019)	120.050 (13.676)	32.700 (2.479)	-	-
	CE	baseline	0.184 (0.030)	0.028 (0.008)	19.445 (4.424)	3.137 (1.161)	-	-
		+DA	0.164 (0.032)	0.043 (0.018)	12.280 (4.623)	4.345 (2.351)	-	-
		+DA+CoLeTra	0.156 (0.031)	0.039 (0.014)	11.375 (4.699)	3.925 (1.842)	-	-
	Dice	baseline	0.176 (0.055)	0.029 (0.011)	17.387 (9.536)	3.320 (1.573)	-	-
		+DA	0.138 (0.021)	0.029 (0.008)	10.278 (3.085)	3.085 (1.047)	-	-
		+DA+CoLeTra	0.133 (0.017)	0.028 (0.008)	10.082 (2.601)	2.968 (1.077)	-	-
CREMI	RWLoss	baseline	0.156 (0.032)	0.027 (0.008)	13.050 (5.225)	3.088 (1.254)	-	-
		+DA	0.146 (0.030)	0.031 (0.011)	10.852 (4.694)	3.353 (1.547)	-	-
		+DA+CoLeTra	0.138 (0.023)	0.030 (0.010)	9.853 (3.719)	3.342 (1.416)	-	-
	cDice	baseline	0.134 (0.021)	0.492 (0.470)	10.562 (3.019)	71.972 (69.785)	-	-
		+DA	0.134 (0.023)	0.473 (0.578)	10.885 (2.803)	68.645 (85.574)	-	-
		+DA+CoLeTra	0.129 (0.016)	0.627 (0.590)	10.377 (1.586)	91.620 (87.311)	-	-
	Warploss	baseline	0.174 (0.053)	0.030 (0.012)	16.995 (9.233)	3.383 (1.650)	-	-
		+DA	0.138 (0.021)	0.029 (0.008)	10.278 (3.085)	3.085 (1.047)	-	-
		+DA+CoLeTra	0.134 (0.019)	0.028 (0.007)	10.088 (2.692)	3.108 (1.070)	-	-
	TopoLoss	baseline	0.182 (0.029)	0.028 (0.008)	19.263 (4.659)	3.105 (1.111)	-	-
		+DA	0.164 (0.032)	0.043 (0.018)	12.280 (4.623)	4.345 (2.351)	-	-
		+DA+CoLeTra	0.162 (0.031)	0.043 (0.018)	11.812 (4.855)	4.325 (2.327)	-	-
Nurwhal	CE	baseline	102.920 (4.846)	65.433 (8.065)	25483.778 (892.552)	19023.778 (2184.153)	6.222 (0.788)	1020.778 (318.252)
		+DA	85.813 (7.831)	56.499 (6.948)	22118.778 (1579.306)	23239.889 (3385.695)	7.951 (0.844)	1848.889 (275.483)
		+DA+CoLeTra	100.249 (5.767)	52.531 (10.965)	25316.444 (1030.693)	23690.222 (5848.199)	7.314 (1.258)	1189.000 (342.287)
	Dice	baseline	92.596 (6.064)	51.323 (6.660)	22747.667 (1848.339)	23081.778 (2526.715)	6.059 (0.559)	725.889 (262.020)
		+DA	63.070 (6.672)	32.536 (4.310)	15833.667 (1254.459)	36768.889 (5455.327)	6.330 (0.638)	736.889 (236.697)
		+DA+CoLeTra	71.400 (5.927)	34.267 (3.433)	17722.111 (1177.585)	34227.111 (5602.781)	6.466 (0.739)	750.111 (188.966)
	RWLoss	baseline	91.591 (5.513)	53.308 (4.826)	22360.778 (1379.857)	22914.889 (2070.941)	5.973 (0.491)	724.778 (139.728)
		+DA	63.129 (5.555)	33.176 (4.272)	15747.333 (995.752)	36398.222 (5491.616)	6.282 (0.634)	656.667 (129.639)
		+DA+CoLeTra	72.948 (5.781)	33.230 (3.642)	18073.000 (1233.530)	34942.778 (5882.784)	6.727 (0.722)	896.556 (229.932)
	cDice	baseline	58.254 (2.755)	33.407 (6.433)	12998.000 (487.383)	31580.667 (2925.908)	28.817 (20.584)	7179.333 (5825.819)
		+DA	28.054 (3.996)	41.048 (9.157)	5274.667 (597.568)	46767.111 (3484.914)	40.694 (36.439)	10896.222 (10530.516)
		+DA+CoLeTra	31.929 (3.276)	41.842 (6.966)	5823.333 (531.701)	47320.111 (3686.082)	28.516 (30.074)	7439.222 (8839.416)
	Warploss	baseline	92.521 (5.132)	51.846 (6.788)	22727.889 (1575.938)	22759.111 (2657.958)	5.873 (0.618)	733.889 (259.979)
		+DA	63.570 (6.586)	32.962 (3.534)	15931.667 (1356.138)	36482.222 (5593.270)	6.279 (0.597)	763.667 (202.555)
		+DA+CoLeTra	72.541 (3.758)	33.227 (3.755)	17863.556 (598.402)	34594.889 (4623.187)	6.737 (0.605)	872.333 (132.933)
Nurwhal	TopoLoss	baseline	103.007 (6.213)	63.397 (6.306)	25617.333 (914.328)	19208.778 (1974.309)	6.199 (0.682)	1004.889 (290.994)
		+DA	83.294 (10.438)	52.456 (11.691)	21309.778 (2194.859)	25475.111 (6668.060)	7.576 (1.216)	1561.889 (548.939)
		+DA+CoLeTra	93.221 (9.958)	49.461 (10.552)	23677.444 (2154.987)	24241.667 (3969.347)	7.196 (1.242)	1183.222 (606.389)
	CE	baseline	82.494 (14.838)	7.137 (2.542)	13818.444 (2379.275)	839.333 (751.343)	0.313 (0.064)	49.556 (1.103)
		+DA	151.514 (32.422)	7.057 (1.216)	24430.778 (4492.010)	888.778 (450.626)	0.511 (0.332)	58.000 (39.771)
		+DA+CoLeTra	102.206 (33.086)	6.493 (1.590)	16806.000 (4805.655)	810.778 (396.505)	1.554 (2.187)	255.778 (359.888)
	Dice	baseline	156.026 (20.537)	5.544 (1.097)	25869.667 (2713.092)	520.556 (409.210)	0.553 (0.465)	68.889 (30.413)
		+DA	124.166 (33.139)	5.777 (1.351)	20969.444 (4201.928)	736.556 (511.386)	0.411 (0.223)	44.556 (17.321)
		+DA+CoLeTra	146.443 (69.581)	5.867 (1.409)	24830.111 (10180.901)	765.111 (495.148)	1.287 (1.738)	191.111 (241.525)
	RWLoss	baseline	108.196 (112.014)	8.022 (1.891)	17789.111 (16530.243)	1092.556 (486.083)	0.357 (0.101)	40.778 (7.889)
		+DA	44.343 (30.800)	6.361 (1.913)	8112.333 (4885.627)	718.778 (448.861)	0.367 (0.104)	36.556 (13.535)
		+DA+CoLeTra	43.891 (28.469)	5.838 (1.621)	7286.222 (5773.509)	673.333 (466.031)	0.370 (0.106)	34.667 (14.849)
	cDice	baseline	28.622 (9.017)	6.221 (1.057)	6167.556 (1601.572)	481.778 (346.257)	0.482 (0.134)	21.333 (16.795)
		+DA	22.621 (17.217)	6.146 (0.744)	5221.111 (3044.832)	620.889 (316.002)	0.356 (0.085)	37.667 (9.777)
		+DA+CoLeTra	16.076 (4.611)	6.153 (0.469)	4159.000 (965.763)	610.333 (335.715)	0.360 (0.084)	39.778 (11.638)
Nurwhal	Warploss	baseline	136.057 (28.535)	5.718 (1.168)	22977.667 (4664.410)	694.111 (483.605)	0.484 (0.346)	58.111 (11.453)
		+DA	124.106 (33.301)	5.782 (1.370)	20966.111 (4222.903)	735.444 (511.870)	0.406 (0.213)	44.111 (17.321)
		+DA+CoLeTra	146.526 (69.677)	5.856 (1.440)	24844.000 (10194.729)	765.222 (494.716)	1.281 (1.728)	190.778 (240.948)
	TopoLoss	baseline	126.599 (57.588)	7.707 (3.217)	20388.556 (8153.324)	1007.556 (860.420)	0.329 (0.067)	47.444 (3.272)
		+DA	151.509 (32.427)	7.054 (1.223)	24431.222 (4494.470)	888.667 (451.196)	0.512 (0.334)	57.778 (39.948)
		+DA+CoLeTra	102.090 (33.391)	6.601 (1.610)	16779.111 (4860.278)	822.111 (393.354)	1.614 (2.291)	267.111 (379.808)

Table 7. Betti Errors (AttentionUNet)

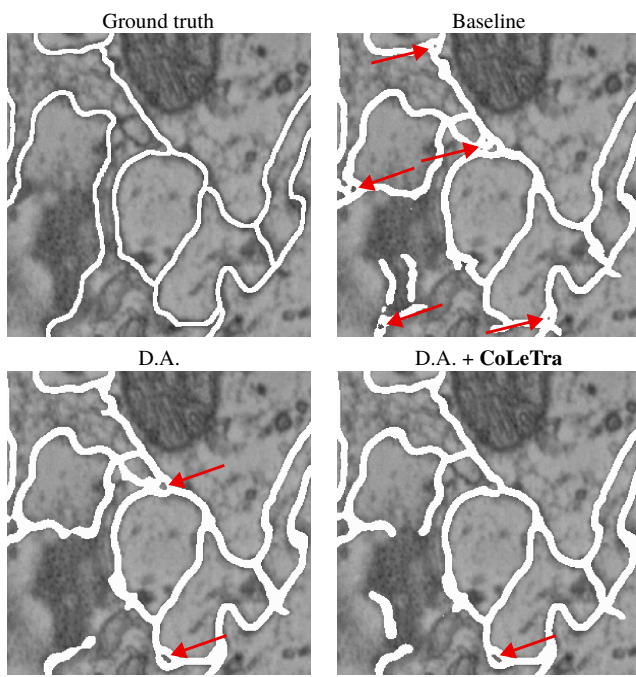


Figure 7. Representative example of the excessive amount of holes produced by models trained without any data augmentation ("baseline").